

Universal Kerr-thermal dynamics of self-injection-locked microresonator dark pulses

Shichang Li,^{1,2,*} Kunpeng Yu,^{1,3,*} Dmitry A. Chermoshentsev,^{4,*} Wei Sun,^{1,†} Jinbao Long,¹ Xiaoying Yan,¹ Chen Shen,^{1,5} Artem E. Shitikov,⁴ Nikita Yu. Dmitriev,⁴ Igor A. Bilenko,^{4,6} and Junqiu Liu^{1,3,‡}

¹International Quantum Academy, Shenzhen 518048, China

²Shenzhen Institute for Quantum Science and Engineering,

Southern University of Science and Technology, Shenzhen 518055, China

³Hefei National Laboratory, University of Science and Technology of China, Hefei 230088, China

⁴Russian Quantum Center, Moscow 143026, Russia

⁵Qaleido Photonics, Shenzhen 518048, China

⁶Faculty of Physics, Lomonosov Moscow State University, Moscow 119991, Russia

Microcombs, formed in optical microresonators driven by continuous-wave lasers, are miniaturized optical frequency combs with small size, weight and power consumption. Leveraging integrated photonics and laser self-injection locking (SIL), compact and robust microcombs can be constructed via hybrid integration of a semiconductor laser with a chip-based microresonator. While the current linear SIL theory has successfully addressed the linear coupling between the laser cavity and the external microresonator, it fails to manage the complicated nonlinear processes, especially regarding to dark-pulse microcomb formation. Here, we investigate – theoretically, numerically and experimentally – the Kerr-thermal dynamics of a semiconductor laser self-injection-locked to an integrated silicon nitride microresonator. We unveil intriguing yet universal dark-pulse formation and switching behaviour with discrete steps, and establish a theoretical model scrutinizing the synergy of laser-microresonator mutual coupling, Kerr nonlinearity, photo-thermal effect. Numerical simulation confirms the experimental result and identifies the origins. Exploiting this unique phenomenon, we showcase an application on low-noise photonic microwave generation with phase noise purified by 23.5 dB. Our study not only add critical insight of pulse formation in laser-microresonator hybrid systems, but also enables all-passive, photonic-chip-based microwave oscillators with high spectral purity.

Optical frequency combs (OFCs)^{1–4} constitute broadband frequency rulers with equidistant lines of continuous-wave (CW) components, and have revolutionized timing, spectroscopy, precision measurement, and testing fundamental physics. While conventional OFCs are constructed with solid-state or fiber mode-locked lasers, microcombs – harnessing enhanced Kerr nonlinearity in ultrahigh- Q optical microresonators driven by CW pumps – have allowed miniaturized OFCs with small size, weight and power consumption^{5,6}. With the emergence and quick maturing of ultralow-loss photonic integrated circuits^{7–10}, as well as heterogeneous and hybrid integration with semiconductor lasers^{11,12}, today micro-

combs can be built entirely on-chip and manufactured in large volume with low cost, catalyzing wide deployment outside laboratories and in space.

Depending on the microresonator’s group velocity dispersion (GVD), there are two types of coherent microcombs. The bright dissipative soliton microcombs^{13–18} require anomalous GVD, while the dark-pulse (also termed “platicon”) microcombs require normal GVD^{19–24}. Compared to solitons, platicons exhibit remarkably higher CW-to-pulse power conversion efficiency^{25,26}, thus are advantageous for coherent optical communication²⁷ and photonic microwave generation²⁸. To initiate platicons, laser self-injection locking (SIL)^{29,30} offers the most robust and effective form, and permits seamless integration of the pump laser and the microresonator^{31–33}. However, while the current *linear* SIL theory and model²⁹ have addressed the linear coupling between the laser cavity and the external microresonator, it fails to manage the complicated *nonlinear* processes in the laser gain media and in platicon formation.

Here, we investigate – theoretically, numerically and experimentally – the Kerr-thermal dynamics of platicon formation using a semiconductor laser self-injection-locked to an integrated silicon nitride (Si_3N_4) microresonator. We unveil an intriguing platicon switching behaviour with discrete steps, allowing operation of platicons in noise-quenched states and immunity to laser noise. Figure 1a illustrates the principle of our study. When a laser-cavity mode is tuned into a resonance mode of the Si_3N_4 microresonator and light is coupled into the microresonator, SIL occurs that locks the laser frequency to the resonance^{29,30} and suppresses the laser linewidth. The linewidth suppression ratio is proportional to Q_r/Q_d , where Q_r/Q_d is the quality factor of the microresonator/laser cavity. Meanwhile, photo-thermal effect^{34–37} induces a global frequency shift of the microresonator’s resonance grid. With sufficient intracavity power, Kerr nonlinearity induces four-wave mixing (FWM)³⁸ that translates photons to other resonances. In microresonators of normal GVD, the synergy of SIL, photo-thermal and Kerr effects ultimately yield platicon formation, as shown in Fig. 1b.

Experimental result. We use a commercial DFB laser chip edge-coupled to a Si_3N_4 microresonator chip^{28,39}, as shown in Fig. 1c. The DFB laser operates at 1549 nm in

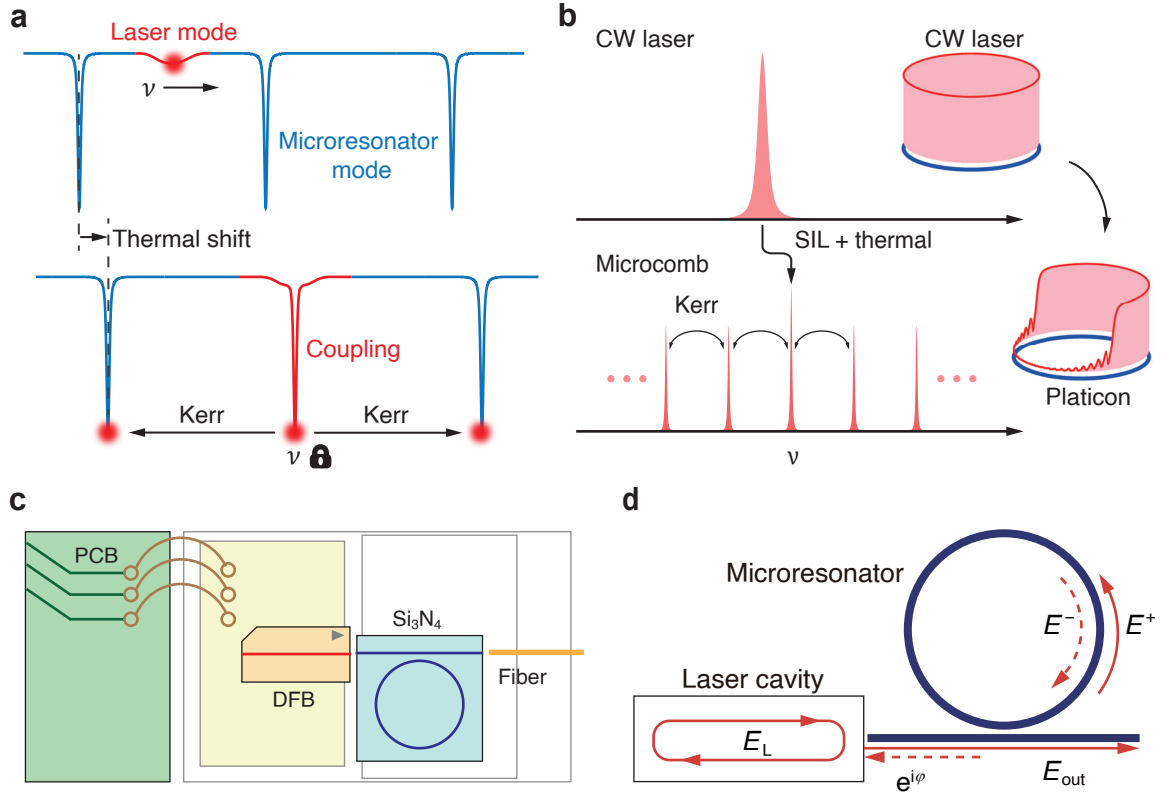


Figure 1. **Principle and schematic of self-injection-locking, Kerr nonlinearity and photo-thermal effect in the laser-microresonator coupled system.** **a.** Frequency-domain picture illustrating the SIL process with the Kerr-thermal effect. **b.** Frequency- and time-domain pictures describing the synergy of SIL, photo-thermal effect and Kerr nonlinearity, which yields narrowing of the pump laser’s linewidth, red-shift of the microresonator’s resonance grid, and formation of a platicon microcomb. **c.** Experimental setup showing the layout of a DFB laser chip edge-coupled to a Si_3N_4 microresonator chip. A home-made printed circuit board (PCB) is used to provide stable current to the laser and to stabilize the laser temperature. Output light from the Si_3N_4 microresonator is collected by a lensed fiber. **d.** Schematic of SIL. E_L : light amplitude in the laser cavity. E^-/E^+ : light amplitude in the clockwise/counter-clockwise direction in the microresonator. E_{out} : light amplitude at the microresonator output. φ : feedback phase of E^- .

the telecommunication C band. It has 1 nm wavelength tuning range and 159 mW output CW power with driving current up to 500 mA. The Si_3N_4 microresonator has 10.7 GHz free spectral range (FSR) and normal GVD. ($D_2 < 0$). The microresonator is critically coupled⁴⁰, with intrinsic quality factor $Q_0 = 23 \times 10^6$. Actual photographs and characterization data of the DFB laser chip and the Si_3N_4 microresonator chip are found in Supplementary Information Note 1.

Figure 1d illustrates the schematic of SIL. Light E_L in the laser cavity is emitted and coupled into the microresonator’s counter-clockwise direction E^+ . Rayleigh scattering in the microresonator reflects a portion of light to the clockwise direction E^- and to the laser cavity. To facilitate SIL, we optimize the edge coupling and the gap distance (thus the feedback phase ϕ) between the two chips. In the SIL regime, we continuously tune the laser current, and monitor the output optical power and frequency from the Si_3N_4 chip. The output light is beaten against a reference laser, and the beat frequency

is recorded. The forward (backward) tuning corresponds to increasing (decreasing) laser current, which decreases (increases) laser frequency.

Figure 2(a, b) shows the experimental data. When SIL occurs, the output power experiences a sudden drop, and the output frequency is shifted. In the SIL regime, we observe decreasing (increasing) output power and frequency with backward (forward) tuning, due to the **photo-thermal effect**^{34–37}. For example, the decreasing output power corresponds to decreasing transmitted power and increasing intra-cavity power. The latter enhances the photo-thermal effect and causes increasing resonance red-shift (towards longer wavelength)³⁴. As the laser frequency is locked to the resonance, the red-shifted resonance drags the laser frequency, leading to decreasing output optical frequency.

Besides, it is apparent that the output optical power and frequency exhibit discrete step features. This is contrary to the conventional, linear SIL model²⁹ showing continuous, nearly anchored tuning curves of power and

frequency. Here, the appearance of these steps are attributed to the **Kerr nonlinearity** in the microresonator with sufficient intra-cavity power. Note that similar discontinuous curves have been observed and characterized in self-injection-locked solitons³¹, while here we observe and characterize these curves for the first time for self-injection-locked platicons. Figure 2c shows the zoom-in profile of the gray-shaded zoom in Fig. 2b. Steps in backward tuning with 320.4 to 321.3 mA laser current are marked with 1 to 4. Typical optical spectra within each step are shown in Fig. 3a, evidencing formation and switching of different platicon states. Distinct fringes are marked with arrows on the spectral envelopes. Numerical simulation of time-domain pulse shapes in Fig. 3c (discussed later) confirms that all these platicon states

are “single platicon” comprising only one dark pulse in the microresonator.

Moreover, identical Kerr-thermal platicon dynamics has also been observed in other two independent SIL setups, where different DFB lasers and 21.3-GHz-FSR Si₃N₄ microresonators are used. Details are found in Supplementary Information Note 1 and 2. These parallel experiments suggest that, our observation of the Kerr-thermal dynamics and discrete steps is universal and independent of the particular lasers or microresonators.

Theory and numerical simulation. To better understand our experimental result, we establish a comprehensive theoretical model harmonizing SIL, Kerr nonlinearity, and photo-thermal effect. The equations describing our laser-microresonator nonlinear system are written as

$$\partial_\tau g_N = J_N - \tilde{\kappa}_N (g_N + g_0) |a_L|^2 \quad (1)$$

$$\partial_\tau a_L = \frac{1}{2} (1 + i\alpha_g) g_N a_L + i e^{i(\alpha_L \tau + \varphi)} \tilde{\kappa}_L b_0 \quad (2)$$

$$\partial_\tau a_\mu = - \left(1 + i \sum_{n=2}^{\infty} \frac{d_n}{n!} \mu^n - iT \right) a_\mu + i \left(\mathcal{F}[|a|^2 a]_\mu + 2a_\mu \sum_{\mu'} |b_{\mu'}|^2 \right) + i \tilde{\beta} b_\mu + i e^{i(-\alpha_L \tau + \varphi)} \tilde{\kappa}_R a_L \delta_{0\mu} \quad (3)$$

$$\partial_\tau b_\mu = - \left(1 + i \sum_{n=2}^{\infty} \frac{d_n}{n!} \mu^n - iT \right) b_\mu + i \left(\mathcal{F}[|b|^2 b]_\mu + 2b_\mu \sum_{\mu'} |a_{\mu'}|^2 \right) + i \tilde{\beta} a_\mu \quad (4)$$

$$\partial_\tau T = \left(k_T \sum_{\mu} (|a_\mu|^2 + |b_\mu|^2) - T \right) / t_h. \quad (5)$$

Derivation of Eq. (1–5) is found in Supplementary Information Note 3. In short, Eq. (1) describes the time evolution of the electron carrier inside the laser cavity, with $\tau = \kappa t/2$, $g_N = 2G_n(N - N_0)/\kappa$, $J_N = 2I/(\kappa e V_L)$, $\tilde{\kappa}_N = 3G_n/(g V_L)$, $g_0 = 2\tilde{G}_0/\kappa$, and $a_L = \sqrt{g \epsilon_0 n_L^2 V_L / (\hbar \omega_L \kappa)} E_L$. Here, κ is the loaded linewidth of the Si₃N₄ microresonator, t is the real time, G_n is the gain coefficient of the active area in the laser cavity, N is the electron carrier density, N_0 is the electron carrier density of the free-running laser with a fixed driving current, I is the driving current on the laser diode, e is the electron charge, V_L is the effective volume of the laser diode’s active area, \tilde{G}_0 is the net gain at N_0 of the gain media in the laser, ϵ_0 is the vacuum permittivity, n_L is the refractive index of the active area, ω_L is the laser cavity resonance frequency, and E_L is the laser amplitude in the laser cavity. The nonlinear coefficient of the Si₃N₄ microresonator is $g = \hbar \omega_0^2 c n_2 / (n_0^2 V_{\text{eff}})$, where \hbar is the reduced Plank constant, ω_0 is the microresonator resonance frequency, c is the speed of light in vacuum, n_2 is the nonlinear refractive index of Si₃N₄, n_0 is the refractive index of Si₃N₄, and V_{eff} is the effective volume of the Si₃N₄ microresonator.

Equation (2) describes the laser dynamics in the laser cavity, with $\alpha_L = 2\delta\omega_L/\kappa$, $\varphi = \omega_0 t_s$, $\tilde{\kappa}_L = 2\sqrt{\kappa_{\text{ex}} \tau_R T_L T_c n_L V_L} / (\kappa \tau_L \sqrt{n_0 V_{\text{eff}}})$. Here, α_g is the linewidth enhancement factor, $\delta\omega_L$ is the frequency difference between the cold-cavity resonance mode and the microresonator resonance mode, t_s is the time delay between the laser cavity and the microresonator, κ_{ex} is the external coupling rate of the microresonator, τ_R is the light round-trip time in the microresonator, T_L is the light transmission rate at the laser cavity’s output surface, T_c is the light coupling rate into the laser cavity from outside, τ_L is the light round-trip time in the laser cavity, and b_0 is the back-scattered light in the microresonator at the 0th resonance mode.

Equations (3, 4) describe the dynamics of the forward-propagating light a_μ and the back-scattered light b_μ at the μ^{th} resonance mode, with $a_\mu (b_\mu) = \sqrt{g \epsilon_0 n_0^2 V_{\text{eff}} / (\hbar \omega_0 \kappa)} E_\mu^+ (E_\mu^-)$, $d_n = 2D_n/\kappa$, $\tilde{\beta} = 2\beta/\kappa$, and $\tilde{\kappa}_R = 2\sqrt{\kappa_{\text{ex}} T_L T_c n_0 V_{\text{eff}}} / (\kappa \sqrt{\tau_R n_L V_L})$. Here, $E_\mu^+ (E_\mu^-)$ is the laser amplitude of the forward-propagating (back-scattered) light at the μ^{th} resonance mode, D_n is the n^{th} -order dispersion of the microres-

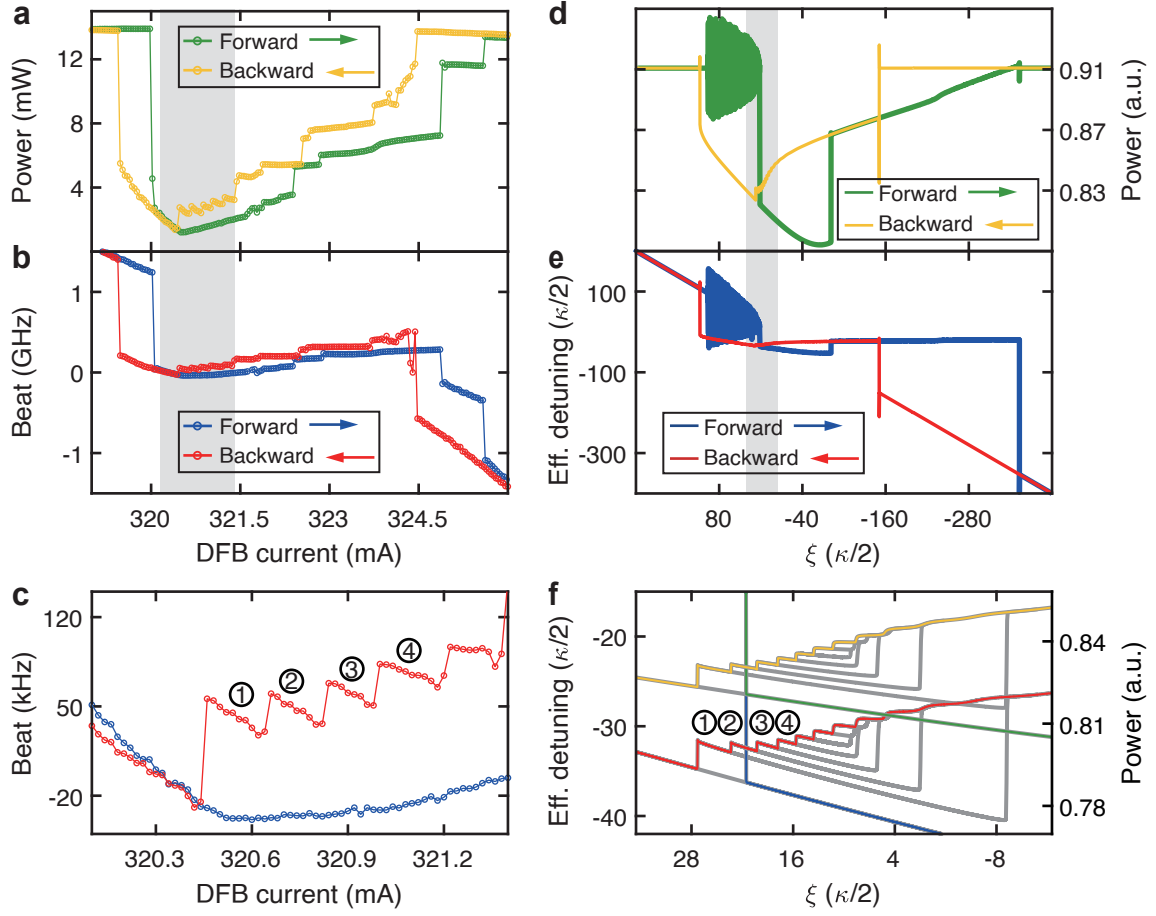


Figure 2. **Experimental result in comparison with numerical simulation.** **a.** Experimentally measured output laser power with forward (green) or backward (yellow) tuning. **b.** Experimentally measured beat frequency between the output laser and a frequency-fixed reference laser, with forward (blue) or backward (red) tuning. **c.** Zoom-in profiles of the gray-shaded region in **b** with forward (blue) or backward (red) tuning. Discrete steps with backward tuning are numbered with 1 to 4. **d, e.** Numerical simulation results corresponding to experimental data in **a, b**. Horizontal axes are the frequency detuning ξ (in the unit of $\kappa/2$) between the free-running laser frequency and the cold resonance frequency. Effective (Eff.) detuning is the frequency detuning (in the unit of $\kappa/2$) between the locked laser frequency and the cold resonance frequency. **f.** Zoom-in profile of the gray-shaded zoom in **d, e**. Gray curves outlines the full detuning range of platicon steps.

onator, β is the back-scattering ratio between the back-scattered light and the forward-propagating light, and $\mathcal{F}[|a|^2 a]$ ($\mathcal{F}[|b|^2 b]$) represents the Kerr interaction.

Equation (5) describes the evolution of the normalized frequency shift T induced by the temperature in the microresonator, with $k_T = K_T/g$, and $t_h = \kappa\tau_r/2$. Here, K_T is the thermal-induced resonance shift coefficient, and τ_r is the thermal relaxation time.

We further perform numerical simulation of Eq. (1-5) using experimentally obtained or realistic values for each parameter. Details are found in Supplementary Information Note 3. Figure 2(d,e) presents the simulated output optical power and frequency, which agree with the experimental data on both the overall trend (due to the photo-thermal effect) and the platicon steps (due to the Kerr nonlinearity). Figure 2f shows the zoom-in profile of the gray-shaded zoom in Fig. 2(d,e), and highlights the full detuning range of platicon steps with gray curves.

Steps corresponding to those in Fig. 2c are marked. We emphasize that, previous efforts^{24,33,41} to model platicon formation in the SIL regime fail to investigate and analyze the transient behaviour, and thus fail to reveal the step features. Meanwhile, they have also omitted the photo-thermal effect.

Figure 3b presents the simulated platicon spectra for each labelled steps in Fig. 2f. They conform the experimental data in Fig. 3a, not only on the spectral envelopes but also on the number of fringes (marked with arrows). Figure 3c presents the simulated time-domain pulse shapes, revealing that the fringes are related to the oscillating tails at the bottom of the dark pulse (marked with arrows). Unlike the steps of bright dissipative solitons^{31,42}, we demonstrate here that platicon steps can occur even in the single-platicon state, i.e. only one dark pulse in the microresonator.

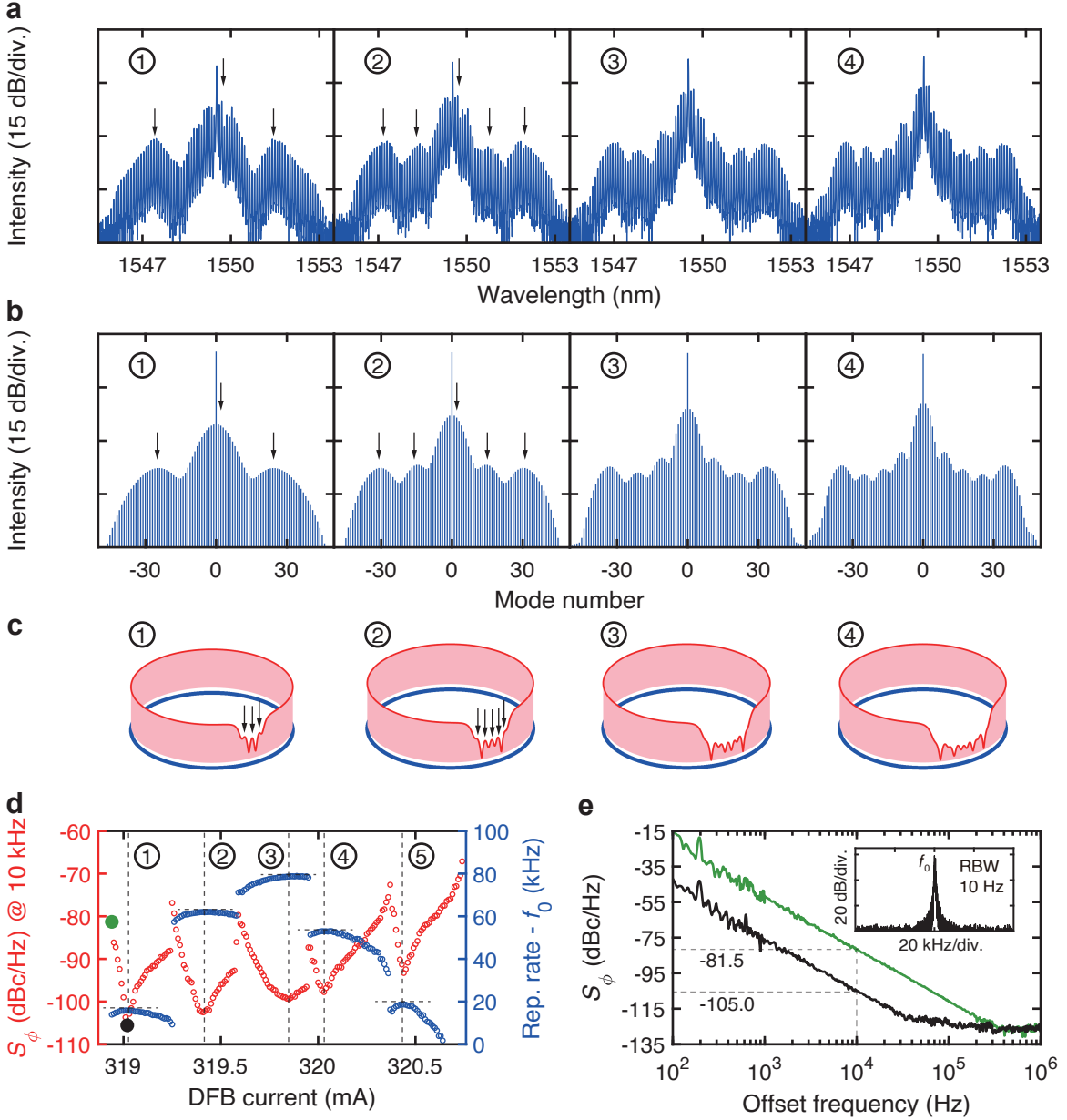


Figure 3. **Optical spectra of different platicon states and the resulted noise-quenching effect.** **a, b.** Experimentally measured **a** and simulated **b** optical spectra of the platicon states labelled in Fig. 2c, f. They agree not only on the spectral envelopes but also on the number of fringes (marked with arrows). **c.** Simulated time-domain pulse shapes of the corresponding platicon states. The fringes, marked with arrows, are related to the oscillating tails at the bottom of the dark pulse. **d.** Measured platicon's repetition rate f_{rep} (blue) and phase noise S_ϕ at 10 kHz Fourier offset frequency (red) of the 10.7-GHz microwave, with backward tuning. $f_0 = 10.68545$ GHz. Vertical dashed lines highlights that the local minimum of S_ϕ coincides with the local maximum of f_{rep} . Horizontal dashed lines highlights that this coincidence is associated with $df_{\text{rep}}/dI = 0$. **e.** Phase noise S_ϕ spectra of the local maximum and minimum points marked with green and black dots in **d**. Phase noise quenching up to 23.5 dB is observed. Inset shows the beatnote of the lowest S_ϕ (black data) with 10 Hz RBW.

Low-noise photonic microwave generation. Finally, we showcase an immediate application of our findings, i.e. to generate low-noise photonic microwave which are ubiquitously deployed in modern information systems for wireless communication, timing and radar. Photonic microwave – microwave synthesized via photonics – allows unrivalled noise performance and

bandwidth breaking the bottleneck of their electronic counterparts^{43–45}. Among various photonics approaches, microcombs, which coherently channel microwave and terahertz frequency to optical frequency, offer an appealing solution for low-noise photonic microwave and millimeter-wave generation^{46–50}. Photodetection of the microcomb's pulse stream creates a microwave whose

carrier frequency corresponds to the microcomb's repetition rate f_{rep} . Several methods have been implemented to further improve the microwave's spectral purity, including the use of an external microwave⁵¹, an auxiliary laser⁵², a transfer comb⁵³, or two-point optical frequency division^{54–56}.

Here we harness the platicon switching dynamics, and demonstrate a unique noise-quenching effect allowing suppression of microwave's phase noise. In contrast to methods mentioned above, our system is free-running, all passive (i.e. without any active locking), and elegantly simple (i.e. without extra RF or laser sources). Experimentally, we collect the output light from the microresonator with a commercial photodetector (PD). The PD converts the dark pulse stream of $f_{\text{rep}} = 10.7$ GHz to a 10.7-GHz microwave in the critical X-band which is dedicated for radar, wireless networks, and satellite communication.

By varying the laser current I within the SIL regime, we monitor the platicon's f_{rep} and phase noise S_ϕ at 10 kHz Fourier offset frequency of the 10.7-GHz microwave, as shown in Fig. 3d. For each step, a local minimum of S_ϕ is observed. Meanwhile, it coincides with the local maximum of f_{rep} , as highlighted with vertical dashed lines in Fig. 3d. This coincidence is due to that, at the local maximum of f_{rep} , we have $df_{\text{rep}}/dI = 0$, as highlighted with horizontal dashed lines in Fig. 3d. Therefore, f_{rep} becomes insensitive to current-noise-induced laser frequency jitter, resulting in the lowest S_ϕ . More analysis of this coincidence is found in Supplementary Information Note 4. In fact, this effect is similar to the “quiet point” effect observed in bright dissipative solitons without SIL^{57,58}. The underlying mechanism is attributed to the multi-mode coupling between the laser cavity and the Si₃N₄ microresonator, which causes asymmetric comb-line enhancement or suppression, as shown in Fig. 3a. As a result, f_{rep} depends on the laser frequency (be more specifically, the detuning of the free-running laser frequency to the cold resonance frequency). In our theoretical model, only the pump resonance is considered coupled, i.e. b_0 in Eq. (2). A more precise simulation on the optical spectra should include multi-mode coupling by substituting b_0 with $\sum_{\mu} b_{\mu} e^{i\mu d_1(\tau - \tau_s)}$.

The S_ϕ spectra of the local maximum and minimum points, marked with green and black dots in Fig. 3d, are measured and compared in Fig. 3e, showing 23.5 dB noise reduction. The lowest S_ϕ reaches $-45/ -75/ -105$ dBc/Hz at 0.1/1/10 kHz Fourier offset frequency, and is limited by the shot noise floor at higher frequency offset⁵⁹. Figure 3e inset shows the beatnote of the lowest S_ϕ (black data) with 10 Hz resolution bandwidth (RBW).

Supplementary Information Note 5 illustrates that, such a noise quenching phenomenon has been also observed in parallel experiments with different Si₃N₄ microresonators and DFB lasers, thus is universal.

In conclusion, we unveil an intriguing yet universal Kerr-thermal dynamics of a semiconductor laser self-injection-locked to a Si₃N₄ microresonator where platicon microcombs are formed. We experimentally observe and characterize the platicon switching dynamics with discrete steps. We further establish a comprehensive theoretical model cooperating the laser-cavity dynamics, the platicon formation dynamics, the photo-thermal dynamics, and the mutual coupling between them. Numerical simulation confirms the experimental result, and illuminates that the platicon switching phenomenon is originated from the synergy of SIL, Kerr nonlinearity and the photo-thermal effect. Exploiting this finding, we showcase low-noise microcomb-based microwave generation. Via operation of platicons with specific laser current, we achieve 23.5 dB phase noise quenching of the 10.7-GHz microwave carrier. Our study not only add critical insight of pulse formation in linear-and-nonlinear-coupled laser-microresonator systems, but also offer a neat solution for photonic-chip-based microwave oscillators with high spectral purity, ideal for microwave photonics, coherent optical communication, analog-to-digital conversion, wireless links, and radar.

Acknowledgments: We thank Baoqi Shi for characterizing the Si₃N₄ chips, and Zhiyang Chen for assistance in the experiment. We acknowledge support from the National Natural Science Foundation of China (Grant No.12261131503, 12404436), Innovation Program for Quantum Science and Technology (2023ZD0301500), Guangdong-Hong Kong Technology Cooperation Funding Scheme (Grant No. 2024A0505040008), Shenzhen-Hong Kong Cooperation Zone for Technology and Innovation (HZQB-KCZYB2020050), and Shenzhen Science and Technology Program (Grant No. RCJC20231211090042078). Russian Quantum Center was supported by RSF grant (23-42-00111). The DFB lasers were fabricated by Shenzhen PhotonX Technology Co. Ltd. and Henan Shijia Photons Technology Co. Ltd. Silicon nitride chips were fabricated by Qaleido Photonics.

Author contributions: W. S. and J. Liu conceived the experiment. S. L., W. S., J. Long and X. Y. built the experimental setup. S. L. and W. S. performed the experiments and analyzed the data, with the assistance from A. E. S. and N. Y. D.. K. Y., D. A. C., and W. S. developed the theory and performed the simulation, with the assistance from A. E. S., N. Y. D. and I. A. B.. C. S. fabricated the Si₃N₄ chips. W. S., S. L., K. Y. and J. Liu wrote the manuscript, with input from others. J. Liu supervised the project.

Data Availability Statement: The code and data used to produce the plots within this work will be released on the repository Zenodo upon publication of this preprint.

* These authors contributed equally to this work.

† sunwei@iqasz.cn

‡ liujq@iqasz.cn

¹ T. Udem, R. Holzwarth, and T. W. Hänsch, *Nature* **416**,

233 (2002).

² S. T. Cundiff and J. Ye, *Rev. Mod. Phys.* **75**, 325 (2003).

³ T. Fortier and E. Baumann, *Communications Physics* **2**, 153 (2019).

- ⁴ S. A. Diddams, K. Vahala, and T. Udem, *Science* **369**, eaay3676 (2020).
- ⁵ P. Del’Haye, A. Schliesser, O. Arcizet, T. Wilken, R. Holzwarth, and T. J. Kippenberg, *Nature* **450**, 1214 (2007).
- ⁶ T. J. Kippenberg, A. L. Gaeta, M. Lipson, and M. L. Gorodetsky, *Science* **361**, eaan8083 (2018).
- ⁷ D. J. Moss, R. Morandotti, A. L. Gaeta, and M. Lipson, *Nature Photonics* **7**, 597 (2013).
- ⁸ A. L. Gaeta, M. Lipson, and T. J. Kippenberg, *Nature Photonics* **13**, 158 (2019).
- ⁹ M. Zhang, C. Wang, R. Cheng, A. Shams-Ansari, and M. Lončar, *Optica* **4**, 1536 (2017).
- ¹⁰ J. Liu, G. Huang, R. N. Wang, J. He, A. S. Raja, T. Liu, N. J. Engelsen, and T. J. Kippenberg, *Nature Communications* **12**, 2236 (2021).
- ¹¹ B. Stern, X. Ji, Y. Okawachi, A. L. Gaeta, and M. Lipson, *Nature* **562**, 401 (2018).
- ¹² C. Xiang, J. Liu, J. Guo, L. Chang, R. N. Wang, W. Weng, J. Peters, W. Xie, Z. Zhang, J. Riemensberger, J. Selvidge, T. J. Kippenberg, and J. E. Bowers, *Science* **373**, 99 (2021).
- ¹³ T. Herr, V. Brasch, J. D. Jost, C. Y. Wang, N. M. Kondratiev, M. L. Gorodetsky, and T. J. Kippenberg, *Nature Photonics* **8**, 145 (2013).
- ¹⁴ X. Yi, Q.-F. Yang, K. Y. Yang, M.-G. Suh, and K. Vahala, *Optica* **2**, 1078 (2015).
- ¹⁵ V. Brasch, M. Geiselmann, T. Herr, G. Lihachev, M. H. P. Pfeiffer, M. L. Gorodetsky, and T. J. Kippenberg, *Science* **351**, 357 (2016).
- ¹⁶ W. Liang, D. Eliyahu, V. S. Ilchenko, A. A. Savchenkov, A. B. Matsko, D. Seidel, and L. Maleki, *Nature Communications* **6**, 7957 (2015).
- ¹⁷ C. Joshi, J. K. Jang, K. Luke, X. Ji, S. A. Miller, A. Klenner, Y. Okawachi, M. Lipson, and A. L. Gaeta, *Opt. Lett.* **41**, 2565 (2016).
- ¹⁸ Y. He, Q.-F. Yang, J. Ling, R. Luo, H. Liang, M. Li, B. Shen, H. Wang, K. Vahala, and Q. Lin, *Optica* **6**, 1138 (2019).
- ¹⁹ X. Xue, Y. Xuan, Y. Liu, P.-H. Wang, S. Chen, J. Wang, D. E. Leaird, M. Qi, and A. M. Weiner, *Nature Photonics* **9**, 594 (2015).
- ²⁰ V. Lobanov, G. Lihachev, T. J. Kippenberg, and M. Gorodetsky, *Opt. Express* **23**, 7713 (2015).
- ²¹ S.-W. Huang, H. Zhou, J. Yang, J. F. McMillan, A. Matsko, M. Yu, D.-L. Kwong, L. Maleki, and C. W. Wong, *Phys. Rev. Lett.* **114**, 053901 (2015).
- ²² P. Parra-Rivas, D. Gomila, E. Knobloch, S. Coen, and L. Gelens, *Optics Letters* **41**, 2402 (2016).
- ²³ E. Nazemosadat, A. Fülöp, O. B. Helgason, P.-H. Wang, Y. Xuan, D. E. Leaird, M. Qi, E. Silvestre, A. M. Weiner, and V. Torres-Company, *Phys. Rev. A* **103**, 013513 (2021).
- ²⁴ H. Wang, B. Shen, Y. Yu, Z. Yuan, C. Bao, W. Jin, L. Chang, M. A. Leal, A. Feshali, M. Paniccia, J. E. Bowers, and K. Vahala, *Phys. Rev. A* **106**, 053508 (2022).
- ²⁵ X. Xue, P.-H. Wang, Y. Xuan, M. Qi, and A. M. Weiner, *Laser & Photonics Reviews* **11**, 1600276 (2017).
- ²⁶ J. K. Jang, Y. Okawachi, Y. Zhao, X. Ji, C. Joshi, M. Lipson, and A. L. Gaeta, *Opt. Lett.* **46**, 3657 (2021).
- ²⁷ A. Fülöp, M. Mazur, A. Lorences-Riesgo, Ó. B. Helgason, P.-H. Wang, Y. Xuan, D. E. Leaird, M. Qi, P. A. Andrekson, A. M. Weiner, and V. Torres-Company, *Nature Communications* **9**, 1598 (2018).
- ²⁸ W. Sun, Z. Chen, L. Li, C. Shen, J. Long, H. Zheng, L. Wang, Q. Chen, Z. Zhang, B. Shi, S. Li, L. Gao, Y.-H. Luo, B. Chen, and J. Liu., arXiv **2403.02828** (2024).
- ²⁹ N. M. Kondratiev, V. E. Lobanov, A. V. Cherenkov, A. S. Voloshin, N. G. Pavlov, S. Koptyaev, and M. L. Gorodetsky, *Optics Express* **25**, 28167 (2017).
- ³⁰ N. M. Kondratiev, V. E. Lobanov, A. E. Shitikov, R. R. Galiev, D. A. Chermoshentsev, N. Y. Dmitriev, A. N. Danilin, E. A. Lonshakov, K. N. Min’kov, D. M. Sokol, S. J. Cordette, Y.-H. Luo, W. Liang, J. Liu, and I. A. Bilenko, *Frontiers of Physics* **18**, 21305 (2023).
- ³¹ A. S. Voloshin, N. M. Kondratiev, G. V. Lihachev, J. Liu, V. E. Lobanov, N. Y. Dmitriev, W. Weng, T. J. Kippenberg, and I. A. Bilenko, *Nature Communications* **12**, 235 (2021).
- ³² W. Jin, Q.-F. Yang, L. Chang, B. Shen, H. Wang, M. A. Leal, L. Wu, M. Gao, A. Feshali, M. Paniccia, K. J. Vahala, and J. E. Bowers, *Nature Photonics* **15**, 346 (2021).
- ³³ G. Lihachev, W. Weng, J. Liu, L. Chang, J. Guo, J. He, R. N. Wang, M. H. Anderson, Y. Liu, J. E. Bowers, and T. J. Kippenberg, *Nature Communications* **13**, 1771 (2022).
- ³⁴ T. Carmon, L. Yang, and K. J. Vahala, *Opt. Express* **12**, 4742 (2004).
- ³⁵ V. Brasch, M. Geiselmann, M. H. P. Pfeiffer, and T. J. Kippenberg, *Opt. Express* **24**, 29312 (2016).
- ³⁶ X. Yi, Q.-F. Yang, K. Y. Yang, and K. Vahala, *Opt. Lett.* **41**, 2037 (2016).
- ³⁷ M. Gao, Q.-F. Yang, Q.-X. Ji, H. Wang, L. Wu, B. Shen, J. Liu, G. Huang, L. Chang, W. Xie, S.-P. Yu, S. B. Papp, J. E. Bowers, T. J. Kippenberg, and K. J. Vahala, *Nature Communications* **13**, 3323 (2022).
- ³⁸ T. J. Kippenberg, S. M. Spillane, and K. J. Vahala, *Phys. Rev. Lett.* **93**, 083904 (2004).
- ³⁹ Z. Ye, H. Jia, Z. Huang, C. Shen, J. Long, B. Shi, Y.-H. Luo, L. Gao, W. Sun, H. Guo, J. He, and J. Liu, *Photon. Res.* **11**, 558 (2023).
- ⁴⁰ M. H. P. Pfeiffer, C. Herkommer, J. Liu, H. Guo, M. Karpov, E. Lucas, M. Zervas, and T. J. Kippenberg, *Optica* **4**, 684 (2017).
- ⁴¹ N. M. Kondratiev, V. E. Lobanov, E. A. Lonshakov, N. Y. Dmitriev, A. S. Voloshin, and I. A. Bilenko, *Opt. Express* **28**, 38892 (2020).
- ⁴² H. Guo, M. Karpov, E. Lucas, A. Kordts, M. H. P. Pfeiffer, V. Brasch, G. Lihachev, V. E. Lobanov, M. L. Gorodetsky, and T. J. Kippenberg, *Nature Physics* **13**, 94 (2017).
- ⁴³ T. M. Fortier, M. S. Kirchner, F. Quinlan, J. Taylor, J. C. Bergquist, T. Rosenband, N. Lemke, A. Ludlow, Y. Jiang, C. W. Oates, and S. A. Diddams, *Nature Photonics* **5**, 425 (2011).
- ⁴⁴ J. Li, X. Yi, H. Lee, S. A. Diddams, and K. J. Vahala, *Science* **345**, 309 (2014).
- ⁴⁵ X. Xie, R. Bouchand, D. Nicolodi, M. Giunta, W. Hänsel, M. Lezius, A. Joshi, S. Datta, C. Alexandre, M. Lours, P.-A. Tremblin, G. Santarelli, R. Holzwarth, and Y. Le Coq, *Nature Photonics* **11**, 44 (2016).
- ⁴⁶ J. Liu, E. Lucas, A. S. Raja, J. He, J. Riemensberger, R. N. Wang, M. Karpov, H. Guo, R. Bouchand, and T. J. Kippenberg, *Nature Photonics* **14**, 486 (2020).
- ⁴⁷ S. Zhang, J. M. Silver, X. Shang, L. D. Bino, N. M. Ridler, and P. Del’Haye, *Opt. Express* **27**, 35257 (2019).
- ⁴⁸ B. Wang, J. S. Morgan, K. Sun, M. Jahanbozorgi, Z. Yang, M. Woodson, S. Estrella, A. Beling, and X. Yi, *Light: Science & Applications* **10**, 4 (2021).
- ⁴⁹ T. Tetsumoto, T. Nagatsuma, M. E. Fermann, G. Navick-

- aite, M. Geiselmann, and A. Rolland, *Nature Photonics* **15**, 516 (2021).
- ⁵⁰ L. Yao, P. Liu, H.-J. Chen, Q. Gong, Q.-F. Yang, and Y.-F. Xiao, *Optica* **9**, 561 (2022).
- ⁵¹ W. Weng, E. Lucas, G. Lihachev, V. E. Lobanov, H. Guo, M. L. Gorodetsky, and T. J. Kippenberg, *Phys. Rev. Lett.* **122**, 013902 (2019).
- ⁵² R. Liu, C. Zhang, Y. Li, X. Li, J. Lin, B. He, Z. Chen, and X. Xie, *Opt. Lett.* **49**, 754 (2024).
- ⁵³ E. Lucas, P. Brochard, R. Bouchand, S. Schilt, T. Südmeyer, and T. J. Kippenberg, *Nature Communications* **11**, 374 (2020).
- ⁵⁴ I. Kudelin, W. Groman, Q.-X. Ji, J. Guo, M. L. Kelleher, D. Lee, T. Nakamura, C. A. McLemore, P. Shirmohammadi, S. Hanifi, *et al.*, *Nature* **627**, 534 (2024).
- ⁵⁵ S. Sun, B. Wang, K. Liu, M. W. Harrington, F. Tabatabaei, R. Liu, J. Wang, S. Hanifi, J. S. Morgan, M. Jahanbozorgi, *et al.*, *Nature* **627**, 540 (2024).
- ⁵⁶ Y. Zhao, J. K. Jang, G. J. Beals, K. J. McNulty, X. Ji, Y. Okawachi, M. Lipson, and A. L. Gaeta, *Nature* **627**, 546 (2024).
- ⁵⁷ X. Yi, Q.-F. Yang, X. Zhang, K. Y. Yang, X. Li, and K. Vahala, *Nature Communications* **8**, 14869 (2017).
- ⁵⁸ A. C. Triscari, A. Tusnini, A. Tikan, and T. J. Kippenberg, *Communications Physics* **6**, 318 (2023).
- ⁵⁹ A. A. Savchenkov, E. Rubiola, A. B. Matsko, V. S. Ilchenko, and L. Maleki, *Opt. Express* **16**, 4130 (2008).

Supplementary Information to: Universal Kerr-thermal dynamics of self-injection-locked microresonator dark pulses

Shichang Li,^{1,2,*} Kunpeng Yu,^{1,3,*} Dmitry A. Chermoshentsev,^{4,*} Wei Sun,^{1,†} Jinbao Long,¹ Xiaoying Yan,¹ Chen Shen,^{1,5} Artem E. Shitikov,⁴ Nikita Yu. Dmitriev,⁴ Igor A. Bilenko,^{4,6} and Junqiu Liu^{1,3,‡}

¹*International Quantum Academy, Shenzhen 518048, China*

²*Shenzhen Institute for Quantum Science and Engineering,*

Southern University of Science and Technology, Shenzhen 518055, China

³*Hefei National Laboratory, University of Science and Technology of China, Hefei 230088, China*

⁴*Russian Quantum Center, Moscow 143026, Russia*

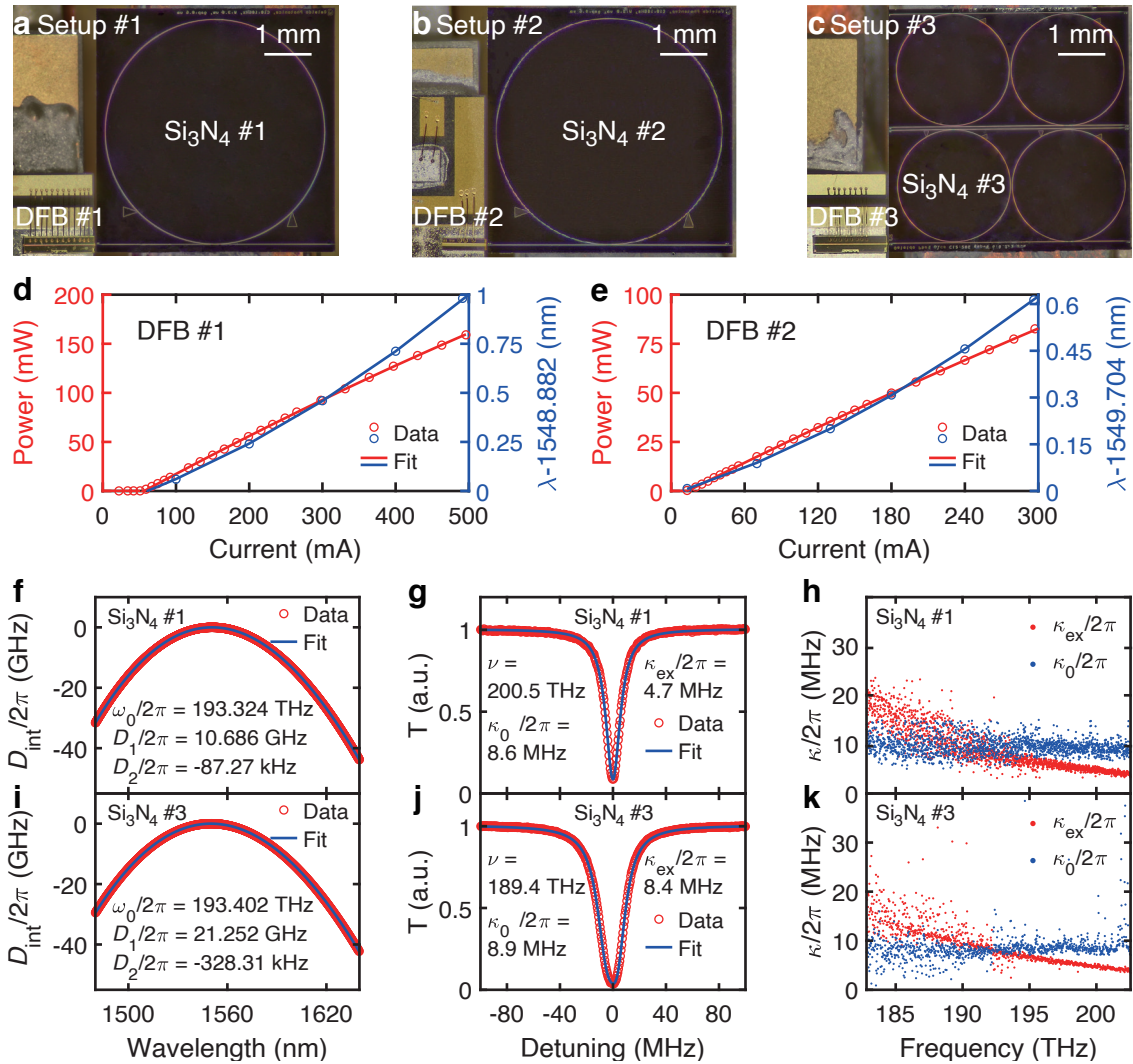
⁵*Qaleido Photonics, Shenzhen 518048, China*

⁶*Faculty of Physics, Lomonosov Moscow State University, Moscow 119991, Russia*

Supplementary Note 1. Characterization of DFB lasers and Si₃N₄ microresonators

The experimental setups (Setup #1-3) used for the observation and verification of the Kerr-thermal dynamics are shown in Supplementary Fig. 1a-c. Two DFB lasers are from Shijia Photons (DFB #1 and DFB #3) and one DFB laser is from Photonx Technology (DFB #2). Two Si₃N₄ microresonators (Si₃N₄ #1 and #2) have the 10.7-GHz FSR and one microresonator (Si₃N₄ #3) has the 21.3-GHz FSR, all fabricated by Qaleido Photonics.

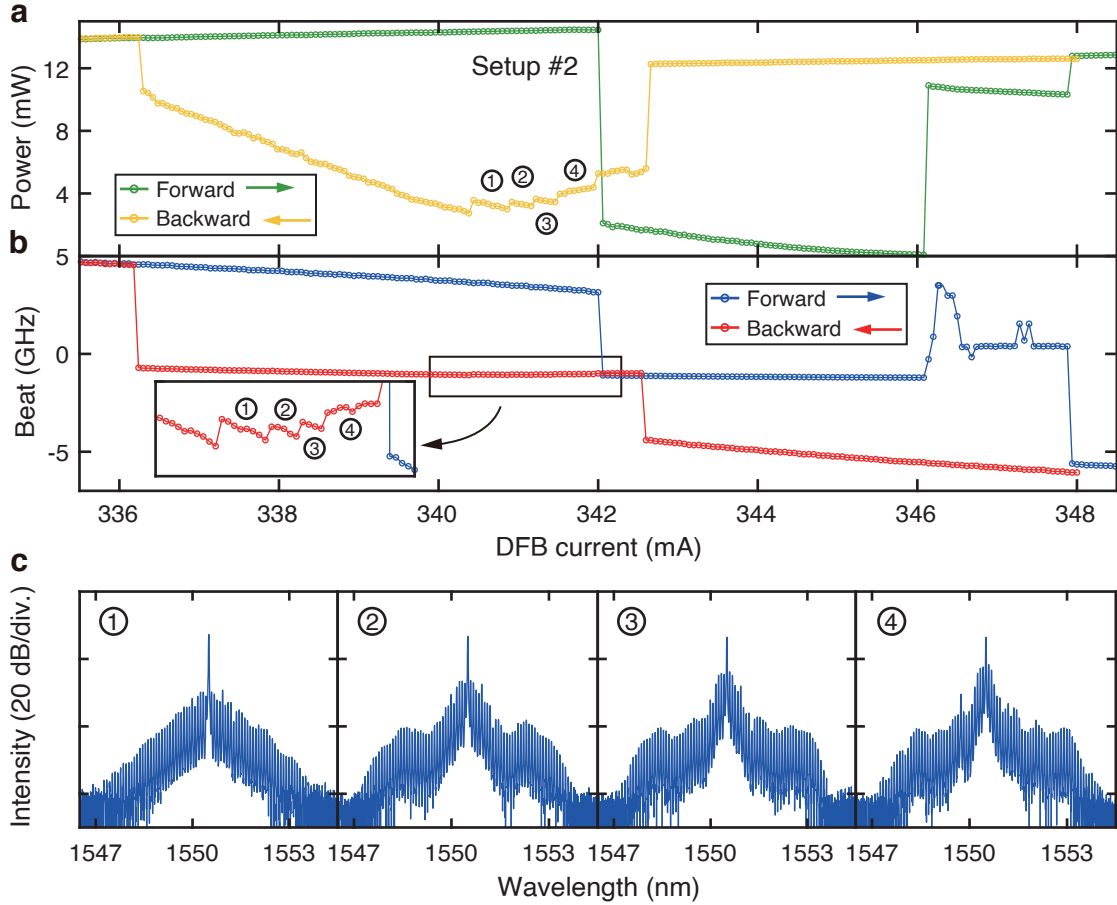
The performances of DFB #1 and DFB #2 are characterized, as shown in Supplementary Fig. 1d and e. As the current is tuned from 0 to 500 mA, the DFB #1's output power increases to 159 mW with the laser threshold of 55 mA. The wavelength can be tuned by 1 nm around 1548.882 nm at the temperature of 30°C. The current of DFB #2 can be tuned up to 300 mA, able to output the maximal power of 83 mW and the wavelength range of 0.6 nm around 1549.704 nm at the temperature of 25°C. The microresonators Si₃N₄ #1 to #3 feature normal group velocity dispersion (GVD), i.e. $D_2 < 0$, which enable the generation of platons. Si₃N₄ #1 and #3 are characterized as shown in Supplementary Fig. 1f-k, where Supplementary Fig. 1f and i show the integrated dispersion D_{int} , Supplementary Fig. 1g and j show the typical transmission resonance, and Supplementary Fig. 1h and k show the loss rate in wide



Supplementary Figure 1: Chips characterization of the three SIL setups. a-c. The photographs of the three different setups (Setup #1-3). Si₃N₄ #1 and #2 are the 10.7-GHz-FSR microresonators from Qaleido Photonics. Si₃N₄ #3 is a 21.3-GHz-FSR microresonator from Qaleido Photonics. DFB #1 and #3 are the DFB lasers from Shijia Photons. DFB #2 is a DFB laser from Photonx Technology. The red(blue) circles show the measured output power(wavelength) of DFB #1 laser in d and DFB #2 laser in e versus the applied current. Solid lines are the corresponding fits. f(i). Measured integrated dispersion of Si₃N₄ #1(#3) microresonator. The microresonator has 10.686(21.252)-GHz FSR and normal GVD of $D_2/2\pi = -87.7(-328.31)$ kHz at the reference frequency $\omega_0/2\pi = 193.324(193.402)$ THz. g(j). The resonance of Si₃N₄ #1(#3) microresonator at 200.5(189.4) THz. The intrinsic loss $\kappa_0/2\pi$ is 8.6(8.9) MHz and the external coupling rate $\kappa_{\text{ex}}/2\pi$ is 4.7(8.4) MHz. Red circles are the measured data and the blue lines are the corresponding fits. h(k). Measured intrinsic (blue dot) and external coupling (red dot) rate of Si₃N₄ #1(#3) microresonator over 20 THz (182.8 THz to 202.6 THz).

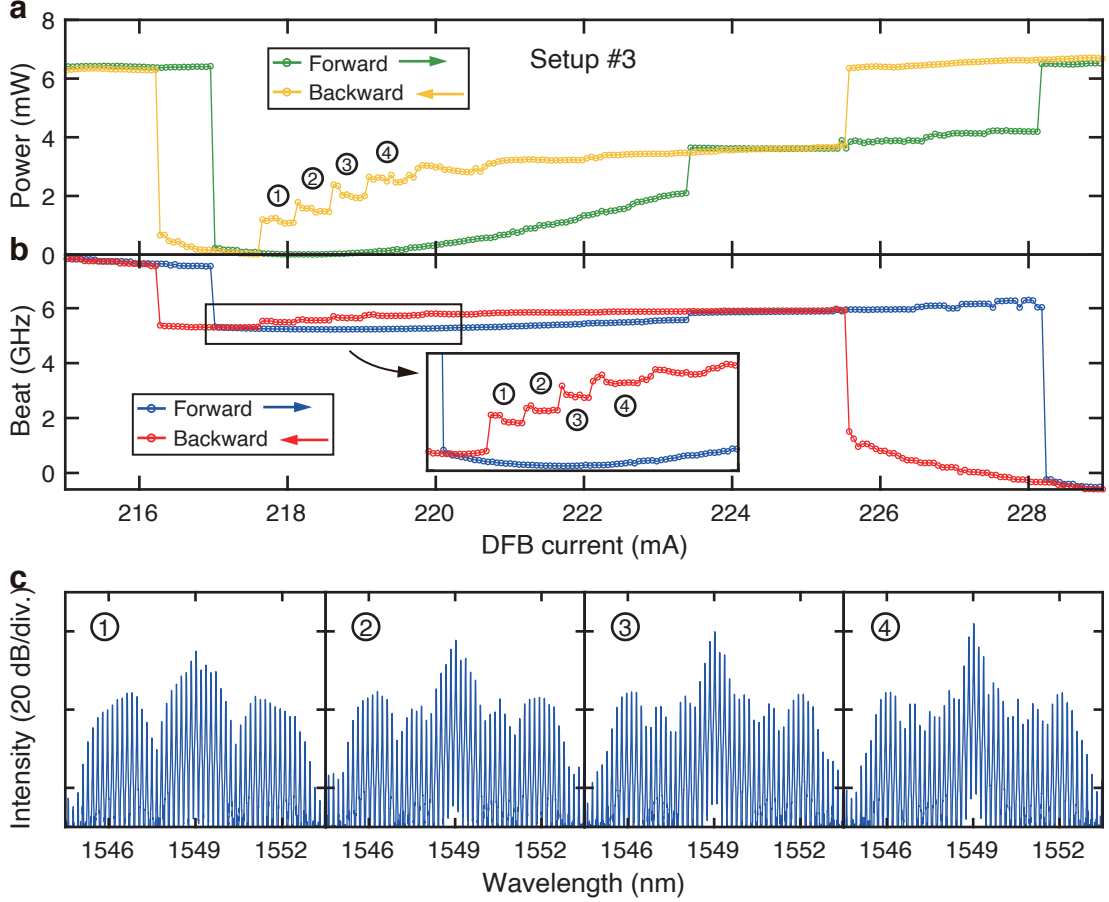
bandwidth. For Si_3N_4 #1 microresonator at frequency $\nu = 200.5$ THz, the intrinsic loss $\kappa_0/2\pi$ and the external coupling rate $\kappa_{\text{ex}}/2\pi$ are fitted as 8.6 MHz and 4.7 MHz respectively, which indicates the intrinsic quality factor $Q_0 = 23 \times 10^6$. For Si_3N_4 #3 microresonator at frequency $\nu = 189.4$ THz, the intrinsic loss and external coupling rates are fitted as 8.9 MHz and 8.4 MHz respectively, which indicates the intrinsic quality factor $Q_0 = 21 \times 10^6$. The comprehensive characterizations of the microresonators are performed by a home-developed vector spectrum analyser¹.

Supplementary Note 2. Universal Kerr-thermal dynamics in Setup #2 and #3



Supplementary Figure 2: SIL dynamics in the second SIL setup. **a.** Measured microresonator output laser power in the forward (green) and backward (yellow) tuning processes. The stair-step features are distinctly presented in the backward tuning process. **b.** Measured beat frequency between the microresonator output laser and the reference laser in the forward (blue) and backward (red) tuning processes. Inset is the zoom-in that shows the stair-step features. **c.** Measured optical spectra of the number-marked steps in **b**.

Except in Setup #1 (DFB #1 + Si_3N_4 #1) in the main text, the Kerr-thermal dynamics are universally found in Setup #2 (DFB #2 + Si_3N_4 #2) and #3 (DFB #3 + Si_3N_4 #3), as shown in Supplementary Fig. 2 and 3. Within the power and beat frequency traces, the platicon steps are observed in the backward tuning process. Supplementary Fig. 2c and 3c display the typical optical spectra corresponding to the numbered steps in Supplementary Fig. 2b and 3b that indicate the switching of the platicon states.



Supplementary Figure 3: SIL dynamics in the third SIL setup. **a.** Measured microresonator output laser power in the forward (green) and backward (yellow) tuning processes. **b.** Measured beat frequency between the microresonator output laser and the reference laser in the forward (blue) and backward (red) tuning processes. All stair-step features are distinctly presented in the backward tuning process of **a** and **b**. **c.** Measured optical spectra of the number-marked steps in **b**.

Supplementary Note 3. Theory derivation and simulation parameters

We begin from the laser rate equations that describe the dynamics of light field and carrier density in the FP laser diode,

$$\partial_t N = \frac{I}{eV_L} - \frac{\epsilon_0 n_L^2}{\hbar \omega_L} G(N) |E_L|^2 \quad (1)$$

$$\partial_t E_L = \left[\frac{1}{2} G(N) + i\delta\omega(N) - \frac{1}{2} \alpha_0 \right] E_L + i e^{i(\delta\omega_{L0}t + \omega_0 t_s)} \frac{\sqrt{\kappa_{\text{ex}} T_R T_L T_c}}{\tau_L} \sqrt{\frac{n_L V_L}{n_0 V_{\text{eff}}}} E_0^- \quad (2)$$

Here N is the carrier density. I is the injection current. V_L is the effective mode volume of the gain area of the laser diode. e is the carrier charge. ϵ_0 is the vacuum permittivity. n_L is the refractive index of the gain area. \hbar is the Planck constant. ω_L is the resonance frequency of the cold laser cavity. $G(N)$ is the gain of the light intensity per unit time of the light field in the gain area, which depends on carrier density N . E_L is the amplitude of the light field in the gain area, which has omitted the phase factor $e^{-i\omega_L t}$ and the transverse part. $\delta\omega(N)$ is the frequency shift caused by the carrier density induced refractive index variation of the gain area. α_0 is the loss factor of the light intensity. $\delta\omega_{L0} = \omega_L - \omega_0$ is the difference between the cold cavity resonant frequency of the laser diode and the microresonator. t_s is the delay time between the microresonator and the laser diode. T_L is the transmission efficiency of the light intensity at the laser cavity's output surface. T_c is the coupling efficiency of the light intensity into the laser cavity from outside. τ_L is the round-trip time of the laser diode. τ_R is the round-trip time of the microresonator. E_0^- is the light amplitude of the 0th mode of the back-scattered light in the microresonator.

When the laser diode runs freely, i.e. without coupling the microresonator, the gain function $G(N)$ must equal to the loss factor α_0 in order to reach a stable state. In the free-running case, we label the carrier density as N_0 , the gain

function as $G_0 = G(N_0)$, and the frequency shift as $\delta\omega(N) = \delta\omega(N_0)$. Then we assume that the carrier density N does not change too far away from N_0 when the laser diode couples with the microresonator. This assumption is practically true because the driving current I does not change too much in the tuning process, as shown in Supplementary Fig. 2 and 3. So, we can use linear approximation $G(N) \approx G_n(N - N_0) + G_0$, $\delta\omega(N)$ and $\delta\omega(N) \approx \delta\omega_0 + \alpha_g G_n(N - N_0)/2$ with α_g being the linewidth enhancement factor. After this approximation, we can rewrite the laser rate equations as follows:

$$\partial_t N = \frac{I}{eV_L} - \frac{\epsilon_0 n_L^2}{\hbar\omega_L} [G_n(N - N_0) + G_0] |E_L|^2 \quad (3)$$

$$\partial_t E_L = \frac{1}{2}(1 + i\alpha_g)G_n(N - N_0)E_L + ie^{i(\delta\omega_L t + \omega_0 t_s)} \frac{\sqrt{\kappa_{\text{ex}}\tau_R T_L T_c}}{\tau_L} \sqrt{\frac{n_L V_L}{n_0 V_{\text{eff}}}} E_0^- \quad (4)$$

Here we have rewrite the amplitude $E_L = E_L e^{i\delta\omega_0 t}$, so $\delta\omega_{L0}$ is replaced by $\delta\omega_L = \delta\omega_{L0} - \delta\omega_0$.

Now we consider the equations describing the dynamics in the microresonator. We use the modified Lugiato-Lefever equation to describe the dynamics of the forward and backward light field in the microresonator as below,

$$\begin{aligned} \partial_t A_\mu^+ = & - \left(\frac{\kappa}{2} + i \sum_{n=2}^{\infty} \frac{D_n}{n!} \mu^n - iT_h \right) A_\mu^+ + ig \left(\mathcal{F}[|A^+|^2 A^+]_\mu + 2A_\mu^+ \sum_{\mu'} |A_{\mu'}^-|^2 \right) + i\beta A_\mu^- \\ & + ie^{i(-\delta\omega_L t + \omega_L t_s)} \sqrt{\frac{\kappa_{\text{ex}} T_L T_c}{\tau_R}} \sqrt{\frac{n_0 V_{\text{eff}}}{n_L V_L}} A_L \delta_{0\mu} \end{aligned} \quad (5)$$

$$\partial_t A_\mu^- = - \left(\frac{\kappa}{2} + i \sum_{n=2}^{\infty} \frac{D_n}{n!} \mu^n - iT_h \right) A_\mu^- + ig \left(\mathcal{F}[|A^-|^2 A^-]_\mu + 2A_\mu^- \sum_{\mu'} |A_{\mu'}^+|^2 \right) + i\beta A_\mu^+ \quad (6)$$

$$\partial_t T_h = \frac{1}{\tau_h} \left(K_T \sum_{\mu} (|A_\mu^+|^2 + |A_\mu^-|^2) - T_h \right). \quad (7)$$

Here $A_\mu^\pm = \mathcal{F}[A^\pm]_\mu = \int d\phi A^\pm e^{i\mu\phi}$, A^\pm is the forward/backward amplitude which has been rescaled as

$$A^\pm = \sqrt{\frac{\epsilon n_0^2}{2\hbar\omega_0} V_{\text{eff}}} E^\pm. \quad (8)$$

Also, E_L is rescaled to be A_L as

$$A_L = \sqrt{\frac{\epsilon_0 n_L^2}{\hbar\omega_L} V_L} E_L \quad (9)$$

where $\kappa = \kappa_0 + \kappa_{\text{ex}}$ is the loaded linewidth of the microresonator with κ_0 representing the intrinsic loss and κ_{ex} representing the external coupling rate, D_n is n^{th} order dispersion coefficient, $g = \hbar\omega_0^2 c n_2 / (n_0^2 V_{\text{eff}})$ is nonlinear coefficient, n_2 is Kerr coefficient, β is Rayleigh scattering coefficient, T_h is the resonant frequency shift caused by thermal effect, K_T is the thermal-induced frequency shift coefficient, and τ_h is thermal relaxation time. Note that we have rescaled the laser amplitude E_L as A_L , so the laser rate equations become

$$\partial_t N = \frac{I}{eV_L} - \frac{1}{V_L} [G_n(N - N_0) + G_0] |A_L|^2 \quad (10)$$

$$\partial_t A_L = \frac{1}{2}(1 + i\alpha_g)G_n(N - N_0)A_L + ie^{i(\delta\omega_L t + \omega_0 t_s)} \frac{\sqrt{\kappa_{\text{ex}}\tau_R T_L T_c}}{\tau_L} \sqrt{\frac{n_L V_L}{n_0 V_{\text{eff}}}} A_0^- \quad (11)$$

By defining $\tau = \kappa t/2$, $a = \sqrt{2g/\kappa} A^+$, $b = \sqrt{2g/\kappa} A^-$, $a_L = \sqrt{2g/\kappa} A_L$, $g_N = 2G_n(N - N_0)/\kappa$, $T = 2T_h/\kappa$, we normalize the equations above as

$$\partial_\tau g_N = J_N - \tilde{\kappa}_N (g_N + g_0) |a_L|^2 \quad (12)$$

$$\partial_\tau a_L = \frac{1}{2} (1 + i\alpha_g) g_N a_L + ie^{i(\alpha_L \tau + \varphi)} \tilde{\kappa}_L b_0 \quad (13)$$

$$\partial_\tau a_\mu = - \left(1 + i \sum_{n=2}^{\infty} \frac{d_n}{n!} \mu^n - iT \right) a_\mu + i \left(\mathcal{F}[|a|^2 a]_\mu + 2a_\mu \sum_{\mu'} |b_{\mu'}|^2 \right) + i\tilde{\beta} b_\mu + ie^{i(-\alpha_L \tau + \varphi)} \tilde{\kappa}_R a_L \delta_{0\mu} \quad (14)$$

$$\partial_\tau b_\mu = - \left(1 + i \sum_{n=2}^{\infty} \frac{d_n}{n!} \mu^n - iT \right) b_\mu + i \left(\mathcal{F}[|b|^2 b]_\mu + 2b_\mu \sum_{\mu'} |a_{\mu'}|^2 \right) + i\tilde{\beta} a_\mu \quad (15)$$

$$\partial_\tau T = \left(k_T \sum_{\mu} (|a_\mu|^2 + |b_\mu|^2) - T \right) / t_h. \quad (16)$$

Here $J_N = 4G_n I / (\kappa^2 e V_L)$, $\tilde{\kappa}_N = G_n / (g V_L)$, $g_0 = 2G_n N_0 / \kappa$, $\alpha_L = 2\delta\omega_L / \kappa$, $\varphi = \omega_0 t_s$, and $\tilde{\kappa}_L$ is defined as

$$\tilde{\kappa}_L = \frac{2}{\kappa} \frac{\sqrt{\kappa_{\text{ex}} \tau_L T_L T_c}}{\tau_L} \sqrt{\frac{n_L V_L}{n_0 V_{\text{eff}}}} \quad (17)$$

$d_n = 2D_n / \kappa$, $\tilde{\beta} = 2\beta / \kappa$, $\tilde{\kappa}_R$ is defined as:

$$\tilde{\kappa}_R = \frac{2}{\kappa} \sqrt{\frac{\kappa_{\text{ex}} T_L T_c}{\tau}}_R \sqrt{\frac{n_0 V_{\text{eff}}}{n_L V_L}} \quad (18)$$

$k_T = K_T / g$, and $t_h = \kappa \tau_h / 2$.

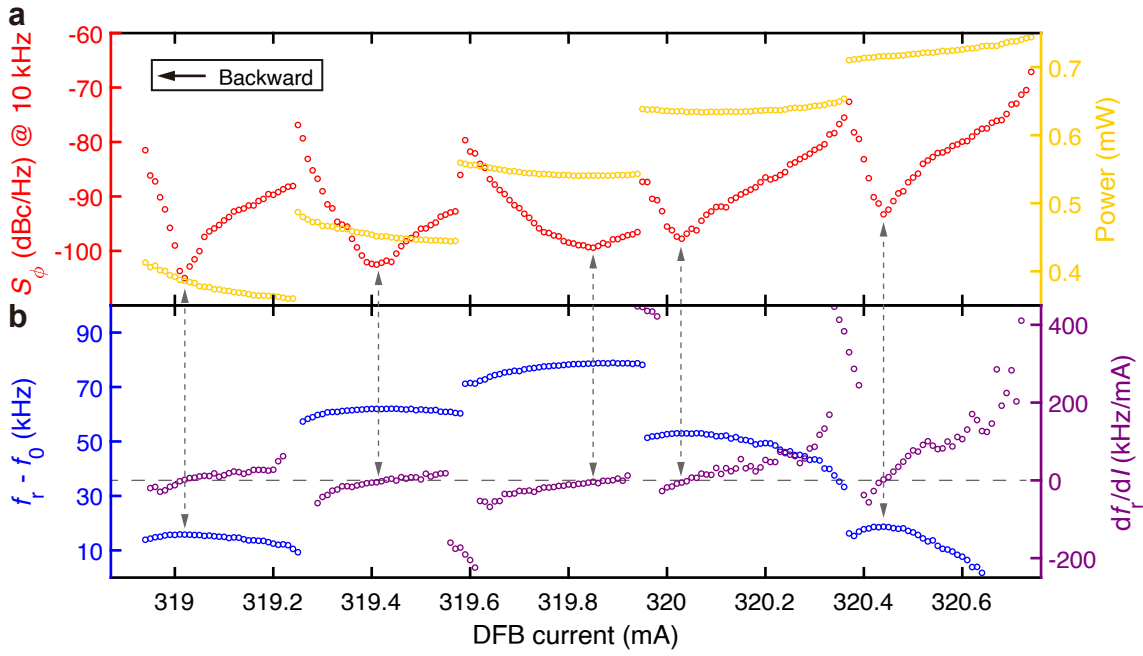
The parameters values for the simulation results in the main text are listed in Supplementary Table I. A complete simulation usually needs hundreds of hours because the nonlinear process can not be proceeded by parallel computing.

Supplementary Table I: Parameters values in simulation

I (mA)	$\kappa/2\pi$ (MHz)	e (C)	V_L (m ³)	G_n (m ³ /s)	\hbar (J·s)	$\omega_0/2\pi$ (THz)	c (m/s)	n_2 (m ² /W)
316	18.6	1.6×10^{-19}	1.05×10^{-14}	2.38×10^{-12}	1.05×10^{-34}	193.48	299792458	9.6×10^{-19}
n_0	V_{eff} (m ³)	N_0 (m ⁻³)	α_g	$\omega_L/2\pi$ (THz)	φ (rad)	κ_{ex} (MHz)	T_L	T_c
1.937	4.58×10^{-14}	1.42×10^{21}	270	193.48	0.24	11.9	0.1	0.3
n_L	τ_L (s)	$D_1/2\pi$ (GHz)	$D_2/2\pi$ (kHz)	$D_3/2\pi$ (Hz)	β	τ_R (s)	K_T (rad/s/J)	τ_h (s)
3.8	3.8×10^{-11}	10.697	-89.3	11.5	0.6	9.3×10^{-11}	5.8	3×10^{-7}

Supplementary Note 4. Analysis on noise quenching

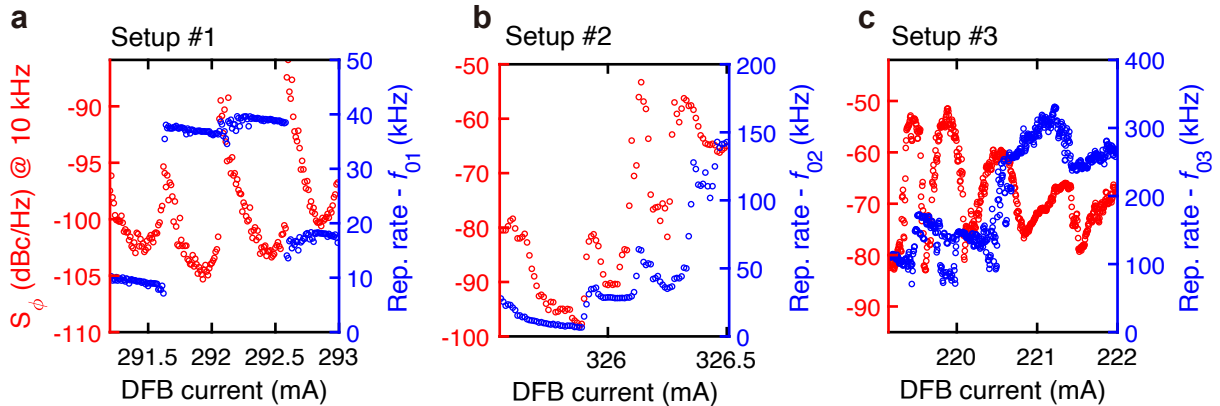
Supplementary Fig. 4 shows five different platicon states accessed in the backward tuning as described in the main text (Setup #1: DFB #1 + Si₃N₄ #1). Upon photodetection of the platicon pulse stream, the PD outputs microwaves of carrier frequency corresponding to the platicon's repetition rate of $f_r \approx 10.7$ GHz. We continuously tune the DFB current, and simultaneously monitor the platicon's optical power (proportional to the PD's DC output voltage, yellow data), the microwave phase noise (red data) and the repetition rate f_r (blue data). The switching dynamics among different platicon states endows discrete step features in the traces of PD's DC voltage. Within each platicon state, a local minimum of S_ϕ is found, providing phase noise quenching. Interestingly yet comprehensibly, such local minima of S_ϕ always coincide with local maxima of f_r , where f_r has null dependence to the DFB current I , i.e. $df_r/dI = 0$ as marked of the (purple data). It means that f_r is insensitive to current fluctuation and noise that is one of the main factor determining the laser frequency noise. Gray dashed arrows highlight the coincidence of local minima of S_ϕ , local maxima of f_r , and $df_r/dI = 0$ points.



Supplementary Figure 4: The characterization of noise quenching. **a.** Measured platicon optical power (proportional to the PD's DC output voltage, yellow dots) and the microwave phase noise S_ϕ at 10 kHz Fourier offset frequency of the repetition rate f_r (red dots). **b.** Measured repetition rate f_r (blue dots) and the derivative of f_r to the DFB current (i.e. df_r/dI , purple dots). $f_0 = 10.685450$ GHz is a frequency offset. Within each platicon state, the gray dashed arrows across **a** and **b** highlight the noise-quenching states, where the local minima of S_ϕ always coincide with the local maxima of f_r and $df_r/dI = 0$ points.

Supplementary Note 5. Universal noise quenching dynamics in different conditions

The noise quenching phenomenon on platicon repetition rate can be found in different Si_3N_4 microresonator resonance modes and different setups, as shown in Supplementary Fig. 5. Supplementary Fig. 5a shows the noise quenching dynamics on the same setup (Setup #1: DFB #1 + Si_3N_4 #1) as in the main text but in a Si_3N_4 resonance mode with higher frequency (lower DFB current). DFB #1 is from Shijia Photons and the FSR of the Si_3N_4 #1 microresonator is 10.7 GHz. Supplementary Fig. 5b shows the noise quenching dynamics in Setup #2 (DFB #2 + Si_3N_4 #2) with the PhotonX Technology DFB laser (DFB #2) and the FSR of the Si_3N_4 microresonator being 10.7 GHz (Si_3N_4 #2). Setup #3 (DFB #3 + Si_3N_4 #3) contains the Shijia Photons DFB laser (DFB #3) and the 21.3-GHz-FSR Si_3N_4 microresonator (Si_3N_4 #3), which also shows distinct noise quenching dynamics. All the Si_3N_4 microresonators are



Supplementary Figure 5: Universal noise quenching dynamics. The red circles represent the phase noise of the platicon repetition rate at 10 kHz Fourier offset frequency. The blue circles represent the platicon repetition rate. Setup #1 (DFB #1 + Si_3N_4 #1) in **a** is the same setup as in the main text with Shijia Photons DFB laser and the 10.7-GHz-FSR Si_3N_4 microresonator. $f_{01} = 10.685340$ GHz. Setup #2 (DFB #2 + Si_3N_4 #2) in **b** contains the PhotonX Technology DFB laser and the 10.7-GHz-FSR Si_3N_4 microresonator. $f_{02} = 10.676660$ GHz. Setup #3 (DFB #3 + Si_3N_4 #3) in **c** contains the Shijia Photons DFB laser and the 21.3-GHz-FSR Si_3N_4 microresonator. $f_{03} = 21.371100$ GHz.

from Qaleido Photonics wiht normal GVD permitting platicon generation, as characterized in Supplementary Fig. 1.

Supplementary References

* These authors contributed equally to this work.

† sunwei@iqasz.cn

‡ liujq@iqasz.cn

¹ Y.-H. Luo, B. Shi, W. Sun, R. Chen, S. Huang, Z. Wang, J. Long, C. Shen, Z. Ye, H. Guo, and J. Liu, *Light: Science & Applications* **13** (2024).